Astronomy & Astrophysics

Transmission spectroscopy of the hot Jupiter TrES-3 b: Disproof of an overly large Rayleigh-like feature[⋆,⋆⋆]

F. Mackebrandt[1,2], M. Mallonn[1], J. M. Ohlert[3,4], T. Granzer[1], S. Lalitha[5], A. García Muñoz[6], N. P. Gibson[7],
J. W. Lee[8,9], A. Sozzetti[10], J. D. Turner[11], M. Vaňko[12], and K. G. Strassmeier[1]

[1] Leibniz-Institut für Astrophysik Potsdam (AIP), An der Sternwarte 16, 14482 Potsdam, Germany
    e-mail: mackebrandt@mps.mpg.de
[2] Max-Planck-Institut für Sonnensystemforschung, Justus-von-Liebig-Weg 3, 37077 Göttingen, Germany
[3] Michael Adrian Observatorium, Astronomie Stiftung Trebur, 65468 Trebur, Germany
[4] University of Applied Sciences, Technische Hochschule Mittelhessen, 61169 Friedberg, Germany
[5] Tata Institute of Fundamental Research, Homi Bhabha Road, Mumbai 400005, India
[6] Zentrum für Astronomie und Astrophysik, Technische Universität Berlin, Hardenbergstraße 36, 10623 Berlin, Germany
[7] Astrophysics Research Centre, School of Mathematics and Physics, Queens University Belfast, Belfast BT7 1NN, UK
[8] Korea Astronomy and Space Science Institute, 34055 Daejeon, Korea
[9] Astronomy and Space Science Major, Korea University of Science and Technology, 34113 Daejeon, Korea
[10] INAF–Osservatorio Astrofisico di Torino, via Osservatorio 20, 10025 Pino Torinese, Italy
[11] Department of Astronomy, University of Virginia, Charlottesville, VA 22904, USA
[12] Astronomical Institute, Slovak Academy of Sciences, 059 60 Tatranská Lomnica, Slovakia

ABSTRACT

Context. Transit events of extrasolar planets offer the opportunity to study the composition of their atmospheres. Previous work on transmission spectroscopy of the close-in gas giant (TrES)-3 b revealed an increase in absorption towards blue wavelengths of very large amplitude in terms of atmospheric pressure scale heights, too large to be explained by Rayleigh-scattering in the planetary atmosphere.

Aims. We present a follow-up study of the optical transmission spectrum of the hot Jupiter TrES-3 b to investigate the strong increase in opacity towards short wavelengths found by a previous study. Furthermore, we aim to estimate the effect of stellar spots on the transmission spectrum.

Methods. This work uses previously published long slit spectroscopy transit data of the Gran Telescopio Canarias (GTC) and published broad band observations as well as new observations in different bands from the near-UV to the near-IR, for a homogeneous transit light curve analysis. Additionally, a long-term photometric monitoring of the TrES-3 host star was performed.

Results. Our newly analysed GTC spectroscopic transit observations show a slope of much lower amplitude than previous studies. We conclude from our results the previously reported increasing signal towards short wavelengths is not intrinsic to the TrES-3 system. Furthermore, the broad band spectrum favours a flat spectrum. Long-term photometric monitoring rules out a significant modification of the transmission spectrum by unocculted star spots.

Key words. planets and satellites: atmospheres – stars: individual: TrES-3 – methods: data analysis – techniques: spectroscopic – techniques: photometric

1. Introduction

Transiting exoplanets present a unique opportunity to probe the upper regions of their atmospheres. During transit, the stellar light passes through the annulus of the planet's atmosphere and

is absorbed until an optical depth of about unity. Wavelength-dependent variations in the atmospheres optical depth cause variations in that transit depth. This yields information about atoms, molecules, and condensates in the outer (optically thin) region of the planetary atmosphere.

The magnitude of the wavelength dependence of the transit depth can be approximated by the area of the planetary atmosphere compared to the area of the star. Therefore, the observability of the transmission signal is maximised for planets with a large planet-to-star radius ratio and a large atmospheric pressure scale height. The majority of atmospheric characterisations have been accomplished for hot Jupiter exoplanets (Sing et al. 2016). However, observations of transmission spectra of Neptune-sized planets (e.g. Fraine et al. 2014) and super-Earths (e.g. Kreidberg et al. 2014) have also been published.

The vertical extent of the atmospheric annulus probed by transmission spectroscopy at optical wavelengths is about five

to ten scale heights for gas giants (Seager et al. 2009; Burrows 2014; Madhusudhan et al. 2014). This signal size is predicted for atomic and molecular absorption in cloud/haze-free atmosphere models as well as for Rayleigh-scattering in hazy atmospheres (Fortney et al. 2010; Miller-Ricci & Fortney 2010; Wakeford & Sing 2015). The vast majority of detected transmission signals is in agreement with this amplitude or lower (e.g. Sing et al. 2016; Sedaghati et al. 2016; Kreidberg et al. 2015; Fraine et al. 2014; Nikolov et al. 2016; Gibson et al. 2017). Stronger amplitudes measured in the UV can be understood as Lyα absorption in the planetary escaping exosphere (Ehrenreich et al. 2015; Vidal-Madjar et al. 2003). However, measured transmission signals of more than ten scale heights amplitude at optical wavelengths have been proposed (Southworth et al. 2015; Mancini et al. 2014; Turner et al. 2016; Parviainen et al. 2016). The physical interpretation of these results is challenging, because according to our current understanding these signals cannot entirely be caused by the planetary atmosphere. Does stellar activity influence the measurements (Oshagh et al. 2013), or does contamination from a nearby star play a role (Southworth & Evans 2016)? Are the values of the planetary scale height underestimated, which would point to a severely wrong estimation of planetary parameters, or are the uncertainties in the transmission spectroscopy measurements underestimated? Could there be missing physics in the modelling of exoplanet transmission spectra?

Ground-based transmission spectroscopy is often conducted with transit observations in low-resolution (e.g. Sing et al. 2012; Lendl et al. 2016; Mallonn & Strassmeier 2016) or high-resolution spectroscopy (e.g. Snellen et al. 2008; Wood et al. 2011). However, very broad spectral features in the planetary spectrum can also be detected by spectrophotometry using multiple broad band filters (Mancini et al. 2013; Nascimbeni et al. 2015; Kirk et al. 2016; Mallonn et al. 2015b). Examples of such spectral features are an increase in opacity towards blue wavelengths caused by scattering (Nascimbeni et al. 2015) or an increase in opacity towards central optical wavelengths caused by TiO absorption (Evans et al. 2016). The broad filters allow for sub-millimag photon noise in the transit light curves with medium-sized telescopes on the ground (Southworth et al. 2017; Mallonn & Strassmeier 2016; Kirk et al. 2016) and even metre-sized telescopes can contribute significantly to a characterisation of the planet atmosphere when multiple transit light curves of individual filters are analysed together (Mallonn et al. 2015a; Dragomir et al. 2015).

The exoplanet TrES-3 b was discovered by O'Donovan et al. (2007). The planet was identified by two different transit surveys – the Trans-atlantic Exoplanet Survey (TrES) and the Hungarian Automated telescope Network (HATNet). The planet is a massive hot Jupiter of $1.899\,M_{2\!\!\!+}$ with a short orbital period of 1.3 d (Southworth 2011). Attention must be paid to the high impact parameter $b = 0.84$ (Southworth 2011) which indicates an almost grazing orbit.

TrES-3 b is only moderately favourable for transmission spectroscopy because of its rather small scale height compared to other targets observationally investigated. The spectral features of about five scale heights amplitude or less predicted by atmospheric models translate to a variation in transit depth smaller than the precision routinely achieved nowadays in ground-based transmission spectroscopy studies.

Parviainen et al. (2016, hereafter P16) obtained the first transmission spectrum of the hot Jupiter TrES-3 b and reported an overly large Rayleigh-like feature from 650 nm on towards shorter wavelengths. To our knowledge, it is the strongest signal

in units of scale height among all hot Jupiter transmission spectra and so far cannot be theoretically explained (P16). However, P16 analysed only a single transit measurement.

In this work we target the reliability and repeatability of this outstanding transmission signal. Therefore, we reanalyse the Gran Telescopio Canarias (GTC) transit observation used by P16 and homogeneously analyse 36 published and 15 newly observed broad band transit observations in nine band passes from the near-UV until the near-IR to build a broad band spectrophotometry transmission spectrum for comparison. Our aim is to verify whether the signal is intrinsic to the TrES-3 system or rather caused by artefacts in the data or aspects of the data analysis, rather than a detailed atmospheric characterisation.

We performed a photometric long-term monitoring of the host star TrES-3 to search for rotational modulation potentially caused by star spots (Strassmeier 2009). Unocculted star spots on the visible hemisphere of the star influence the transit photometry and therefore the derived transit parameters (Pont et al. 2013). This effect is wavelength dependent and can potentially introduce a slope in the transmission spectrum similar to a spectral scattering signature produced by Rayleigh or Mie scattering by condensate particles (Oshagh et al. 2014). The monitoring program allows us to estimate an upper limit of the spot filling factor and the modification of the measured transit depth.

This paper is structured as follows: Sects. 2 and 3 describe the observations and the data reduction. In Sect. 4, the analysis is presented. The results are reported in Sect. 5, followed by the Discussion and Conclusions in Sect. 6.

2. Observations

The published broad band transit light curve observations are mostly observed in bands of long optical wavelengths. However, the Rayleigh-like feature is pronounced at short and intermediate optical wavelengths. We extended the small sample of published observations in Johnson U, B, and V with 15 new transit light curve observations.

Our new observations along the ones we collected from previous works are summarised in Table A.1. Our analysis is based on more than 50 transit observations in nine different bands.

2.1. Published transit observations

2.1.1. Spectroscopy

P16 published the first transmission spectrum of TrES-3 b, observed with the OSIRIS spectrograph as part of the "GTC exoplanet transit spectroscopy survey" (see also Murgas et al. 2014; Palle et al. 2016). The observation covers a spectral range from 530 nm to 950 nm and was performed on July 8, 2014.

2.1.2. Photometry

We collected 36 transit light curves from the literature obtained in Johnson/Cousin and Sloan filters from the U band to the z' band. The data were originally published by O'Donovan et al. (2007), Gibson et al. (2009), Sozzetti et al. (2009), Colón et al. (2010), Lee et al. (2011), Sada et al. (2012), Vaňko et al. (2013), Jiang et al. (2013), Turner et al. (2013) and Kundurthy et al. (2013). The light curves by Gibson et al. (2009) were obtained with the RISE instrument on the Liverpool Telescope with a transmission from about 500 nm to 700 nm. They are hereafter labelled as "*RISE*".

A transit of TrES-3 b was also observed with the GTC by Colón et al. (2010). They used the OSIRIS instrument in a tunable filter imaging mode. Two quasi simultaneous high-precision light curves were obtained in bandpasses centred at 790.2 nm and 794.4 nm each with a width of 2 nm. Due to the spectral affinity of the light curves, we decided to merge them together. This light curve is hereafter labelled "*792*".

2.2. New transit observations

2.2.1. Calar Alto Observatory

One observation was performed with the 2.2 m telescope at the Calar Alto Observatory (CAHA) with the instrument CAFOS in the *B* band on May 02, 2016. The weather conditions were stated as a photometric night with good transparency and a mean seeing of about 1.2″. The telescope was defocused to an object PSF of about 2.5″ with an integration time of 45 s for each image.

2.2.2. STELLar Activity

STELLar Activity (STELLA) is a robotic observatory with two 1.2 m fully automatic telescopes located at the Teide Observatory on the island of Tenerife with an Echelle spectrograph (SES) and a wide field imager WiFSIP (Strassmeier et al. 2004). It is owned and operated by the Leibniz-Institut für Astrophysik (AIP). Exoplanet transit photometry with WiFSIP was already performed for GJ 1214b, HAT-P-32b and HAT-P-12b (Mallonn et al. 2015a; Seeliger et al. 2014; Teske et al. 2013). We observed six *B* band transits of TrES-3 b with WiFSIP (April 12, 25; May 19; June 01, 05, 18, 2016), as well as three transits in the *z′* band (June 28; July 15, 2016).

2.2.3. Telescopio Nazionale *Galileo*

One observation was performed at the 3.58 m Telescopio Nazionale *Galileo* (TNG) in the *U* band on April 25, 2016. A 2×2 binning mode was used to reduce the read-out-time. The telescope was defocused to spread PSF of the object to about 2.5″. Each image was integrated with 40 s exposures.

2.2.4. Trebur-1m telescope

The Trebur-1 m telescope (T1T) is a 1.2 m telescope operated by a foundation as a part of the Michael Adrian Observatory. It is located in Trebur, near Frankfurt am Main, Germany. TrES-3b has already been observed using T1T (Vaňko et al. 2013). We obtained four new transit observations by the T1T in the *V* band (March 09; April 29; May 02 and 19, 2016) and two observations in the *I* band (July 19; August 25, 2016).

2.2.5. Vainu Bappu Observatory

The Vainu Bappu Observatory (VBO) located in India is owned and operated by the Indian Institute of Astrophysics. It hosts several meter-sized telescopes. We received one observation performed with the 1.3 m JCB-Telescope in the *V* band on April 19, 2016.

2.3. Photometric long-term monitoring

We monitored TrES-3 with STELLA/WiFSIP in 2016 over the course of four months from March 7 to July 10, 2016. Because of the very low $v \sin i$ value of 1.5 km s^{-1} (Sozzetti et al. 2009) we expect a stellar rotation period of >10 days and aimed for a photometric data point approximately every third day. We observed in two filters, Johnson *B* and Johnson *V*, in blocks of three exposures each. The exposure times were 90 and 60 s, respectively. However, due to a failure in the observation setting, only single exposures per filter were obtained in the first month of the campaign. During the time span of about 120 days of the campaign, we obtained data on 43 nights.

3. Data reduction

3.1. Transit data

3.1.1. Spectroscopy

The GTC/OSIRIS data were reduced by routines written in ESO-Midas. The bias value was extracted from the overscan regions per frame and subtracted from the flat, arc lamp, and science frames. We flatfielded the science frames with a master flat created by averaging 100 normalised individual flat frames observed in the morning after the observations. We fitted a polynomial of second order along the centroid of the spectrum in dispersion direction to estimate and correct for the misalignment regarding the pixel rows. The background flux at the stellar spectrum was estimated by a linear interpolation per pixel column between sky stripes on both sides of the spectrum. The one-dimensional (1D) spectra were extracted as the simple flux sum within a certain aperture. We tested which sky stripe and aperture width minimises the scatter in the spectrophotometric light curves. We found wider apertures than P16, namely a 52 pixel-wide aperture for the reference object and a width of 80 pixels for the exoplanet host star. Since the full width at half maximum (FWHM) of the spectral spatial profile varies during the observations, we also tested a FWHM-dependent aperture with different scaling factors. However, this varying aperture width resulted in a higher noise level in the spectrophotometric light curves than the fixed aperture width. The optimal sky stripes had a width of 80 pixels each. We measured a mild drift in dispersion direction relative to the first exposure by fitting a Gaussian profile to the telluric O$_2$ Fraunhofer A line per spectra and approximated it with a second-order polynomial over time. Prior to the wavelength calibration, we subtracted this value that accounted for approximately one pixel at maximum. Then, we used the combined HgAr, Xe, and Ne arc lamp frames taken with the 1″ long slit for wavelength calibration.

3.1.2. Photometry

The reduction of the transit data obtained on STELLA, TNG, CAHA, VBO and T1T was performed homogeneously with a customised ESO-MIDAS pipeline, which calls the photometry software SExtractor (Bertin & Arnouts 1996). A bias value was extracted from the overscan regions and subtracted, and a normalised masterflat was applied to the science images by division. A cosmic ray correction was performed within SExtractor. Aperture photometry was carried out with circular apertures (MAG_APER in SExtractor) and automatically adjusted elliptical apertures (MAG_AUTO in SExtractor). The algorithm repeats the light curve extraction many times with different aperture sizes to determine the aperture that minimises the scatter in the differential target light curve. In the majority of our observations the circular aperture with fixed radius (MAG_APER)
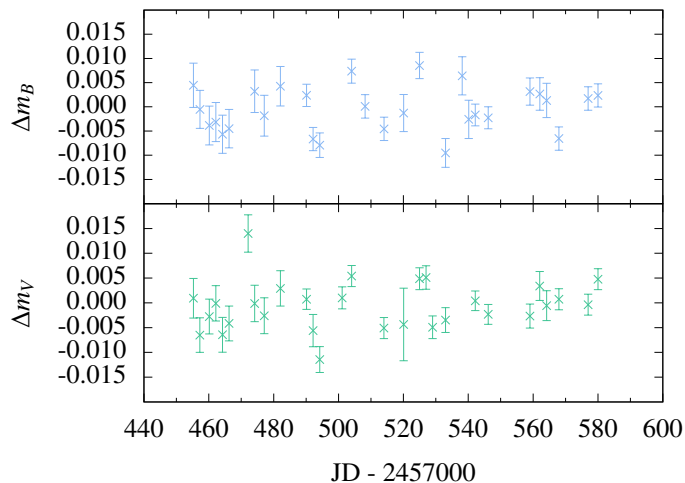
Fig. 1. Monitoring light curve of the host star TrES-3 using STELLA/WiFSIP in Johnson B (*upper panel*) and V (*bottom panel*). Vertical error-bars indicate the 1σ uncertainty.

Fig. 2. Lomb-Scargle periodogram of the monitoring light curves in *B* and *V*. The horizontal lines indicate the false alarm probability (FAP) of 0.1 and 0.01.

yielded a more stable photometry than the flexible elliptical aperture (MAG_AUTO).

We performed differential photometry using the flux sum of multiple stars as a reference light curve. The pipeline looks for a combination of comparison stars which minimises the point-to-point scatter (root mean square, rms) of the target light curve. The comparison stars are weighted according to their individual light curve quality in terms of rms (Broeg et al. 2005). The rms of the target light curve is computed not only on the out-of-transit data but also on the residuals of the entire time series after subtracting a transit fit including a first-order polynomial in time for detrending.

3.2. Long-term photometry

The bias- and flatfield correction was done with the STELLA data-reduction pipeline (Granzer, in preparation). We conducted aperture photometry with SExtractor applying the MAG_AUTO option to automatically adjust elliptical apertures. This option provides the flexibility to account for the varying observing conditions from night to night. We performed differential photometry using the flux sum of multiple stars as a reference light curve. The choice of the comparison stars did not significantly affect the Lomb-Scargle periodograms in the following section. Out of our monitoring data from 43 days, several data points had to be discarded because of instrumental problems or low quality caused by a nearby bright moon. Therefore, we could finally make use of 28 data points in Johnson *B* and 29 data points in Johnson *V* after averaging the three exposures per night (Fig. 1). The rms in both light curves is about 4.8 mmag, which is slightly higher than the typical value of about 2.5 to 3 mmag achieved in similar monitoring campaigns for other exoplanet host stars with the same instrument (Mallonn & Strassmeier 2016; Mallonn et al. 2015b).

4. Analysis

For the analysis of the light curves we used the publicly available software JKTEBOP in version 34 (Southworth et al. 2004)[1]. This code is written in FORTRAN 77 and was originally used to
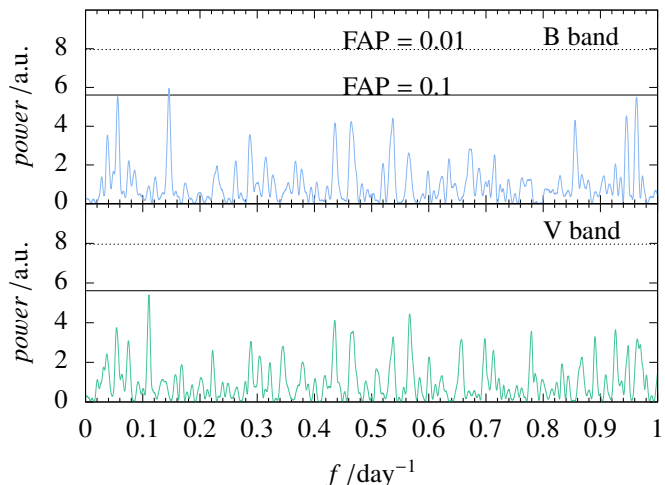
fit models to the light curves of detached eclipsing binary stars but it is also an excellent code for analysing transiting extrasolar systems (Southworth 2008). A Levenberg-Marquardt optimisation algorithm is used to find the best-fitting model. The transit fit parameters consist of the scaled planetary and stellar radius $r_P = R_P/a$ and $r_* = R_*/a$, the orbital inclination i, the transit midtime T_0, the orbital Period P and the host star limb darkening coefficients, as well as an Nth-order polynomial detrending of the light curve as a function of time, with $N \in \{1, 2\}$. The time stamps from all light curves analysed in this work were transferred to BJD_{TDB} following the recommendation of Eastman et al. (2010).

4.1. Orbital parameters

In our analysis of the wavelength dependence of the planet-star radius ratio R_p/R_* we fixed the parameter-scaled stellar radius $r_* = R_*/a$, orbital inclination i, orbital period P, and orbital eccentricity e to common values because they are not wavelength dependent. We fixed the eccentricity to zero (Sozzetti et al. 2009). The orbital period is kept to $P = 1.30618608$ days (Christiansen et al. 2011). To find values for r_* and i we averaged the literature values found by Christiansen et al. (2011), Jiang et al. (2013), O'Donovan et al. (2007), Sozzetti et al. (2009) and Vaňko et al. (2013) with a weighted mean. We discarded the values by Turner et al. (2013) because of their large uncertainties compared to other studies. The individual values and averages are listed in Table 1.

We used these averages as initial values for a white light curve fit of the GTC/OSIRIS spectra. The best-fit transit parameters agree very well to the averaged values and we used the latter one for our subsequent analysis. Using the average ensures suppression of observational systematic errors caused by using many different observations from divers telescopes.

4.2. The stellar limb darkening law

The stellar limb darkening (LD) is a second-order effect modifying the transit shape but it is important for measuring the radius of the planet accurately. In the case of an almost grazing transit, as for TrES-3 b, the transit chord probes the stellar limb, but not the limb to centre brightness variations. In this case,

---

[1] http://www.astro.keele.ac.uk/jkt/codes/jktebop.html

Table 1. Literature values for stellar radius and inclination used for the weighted mean and the result of the white light curve analysis.

Ref.	r_*	$i\,/\,°$	Date of obs.
1	0.1664 ± 0.0204	81.99 ± 0.30	2008-03-06
2		81.73 ± 0.13	
3	0.1685 ± 0.0013	81.81 ± 0.15	2010-05-25
3	0.1679 ± 0.0015	81.75 ± 0.15	2010-06-11
3	0.1684 ± 0.0015	81.83 ± 0.15	2010-06-15
3	0.1670 ± 0.0015	81.95 ± 0.15	2010-06-19
3	0.1691 ± 0.0015	81.89 ± 0.15	2010-06-28
4	0.1675 ± 0.0009	81.95 ± 0.06	2009-05-14
5	0.165 ± 0.003	82.15 ± 0.21	2007-03-26
6	0.1687 ± 0.0016	81.85 ± 0.16	2007-04-24
7	0.1682 ± 0.0032	81.86 ± 0.28	2010-09-06
7	0.1696 ± 0.0027	81.76 ± 0.15	2010-09-06
Average	0.1671 ± 0.0013	81.89 ± 0.12	
White lc	0.167 ± 0.002	81.88 ± 0.18	

References. (1) Christiansen et al. (2011); (2) Gibson et al. (2009); (3) Jiang et al. (2013); (4) Kundurthy et al. (2013); (5) O'Donovan et al. (2007); (6) Sozzetti et al. (2009); (7) Vaňko et al. (2013).

the transit light curve is not suited for fitting the LD coefficients (LDCs) (Müller et al. 2013). Instead, we rely on theoretical calculations of the LDCs. In this work, we use the LDCs published by Claret et al. (2013) and the non-linear four-parameter law introduced by Claret (2000), which provides the most accurate description of the LD compared to other LD laws (Sing 2010). Fixing the LDCs leads to biased values for the radius ratio of less than 0.5 per cent in the case of TrES-3b (Espinoza & Jordán 2015). This is smaller to the uncertainties we achieve in this work. To obtain the LDCs we run a linear interpolation from the tabulated values for the host star parameters T_{eff} = 5650 K and $\log g$ = 4.568 and average each coefficient over the wavelength range of the band. The obtained LDCs are listed in Table 2.

4.3. Third light contamination

Light contamination by unresolved background stars or stellar companions can mimic slopes in the final transmission spectrum of the exoplanet. Ngo et al. (2015) found no companion for TrES-3 within 10 arcsec using the diffraction-limited direct imaging method.

Due to the slit alignment during the GTC observation a faint star (2MASS 17520839+3732378, J = 15.23, K = 14.42) at a distance of about 18 arcsec is projected into the aperture of TrES-3. This star is redder than TrES-3 (2MASS: $J - K$ = 0.81, TrES-3: $J - K$ = 0.407) and thus contributes about 1% of the flux to the red edge of the GTC/OSIRIS spectrum. The estimated modification in the radius ratio is therefore 0.0009. We neglect this contribution because it is smaller than our final uncertainties in the spectrum. Furthermore, the unaffected broad band measurements are in agreement with the GTC data which supports our strategy.

4.4. Light curve fitting

To determine the planetary radius, several model-fitting runs were performed for each individual light curve. The photometric uncertainties determined by SExtractor yield a reduced χ^2 that is always slightly greater than unity, which indicates underestimated photometric uncertainties. We enlarged the error

Table 2. Non-linear limb darkening coefficients after Claret (2000) for the broad band and GTC/OSIRIS light curves used in this work.

Band	c_1	c_2	c_3	c_4
U	1.1981	−2.2854	3.1390	−1.0637
B	0.6263	−0.7628	1.8656	−0.8232
V	0.6943	−0.5840	1.3565	−0.6166
$RISE$	0.8347	−0.7900	1.3819	−0.5936
r'	0.7700	−0.6140	1.1863	−0.5260
R	0.7910	−0.6540	1.1616	−0.5009
792	0.8633	−0.7500	1.0327	−0.4200
I	0.7865	−0.5898	0.9052	−0.3824
z'	0.7621	−0.5362	0.7808	−0.3306
5525 Å	0.8209	−0.8307	1.5294	−0.6622
5775 Å	0.8173	−0.7658	1.4133	−0.6158
6025 Å	0.8200	−0.7317	1.3399	−0.5903
6275 Å	0.8616	−0.8024	1.3246	−0.5644
6525 Å	0.8485	−0.7003	1.1426	−0.4900
6775 Å	0.8581	−0.7636	1.2104	−0.5127
7025 Å	0.8568	−0.7586	1.1734	−0.4929
7275 Å	0.8666	−0.7795	1.1452	−0.4717
7525 Å	0.8567	−0.7518	1.0977	−0.4544
7775 Å	0.8554	−0.7359	1.0502	−0.4336
8025 Å	0.8434	−0.7115	1.0104	−0.4172
8275 Å	0.8436	−0.7208	0.9910	−0.4042
8525 Å	0.8502	−0.7392	0.9671	−0.3865
8775 Å	0.8271	−0.6750	0.8900	−0.3604
9025 Å	0.8305	−0.6903	0.8990	−0.3636
9275 Å	0.8102	−0.6633	0.8832	−0.3610

bars for each light curve by a common factor to produce $\chi^2 = 1$ (Mallonn et al. 2015a). We run a first fit to compute the so-called β-factor, introduced by Winn et al. (2008), which takes systematic noise in the light curves into account (Pont et al. 2006). For the best-fitting model of each individual light curve we calculated the standard deviation of the unbinned residuals σ_1. These residuals were binned into M bins, each with N points and the standard deviation was calculated again for the binned residuals σ_N. For uncorrelated (white) noise we would expect

$$\sigma_N = \frac{\sigma_1}{\sqrt{N}} \sqrt{\frac{M}{M-1}}. \qquad (1)$$

In the presence of correlated (red) noise, σ_N is larger than expected by a factor β. There is a dependence on the bin size and the relevant time scale for transit photometry which is the duration of ingress/egress (Winn et al. 2008). We binned up to 24 min for a total transit duration of about 82 min and applied the β-factor to the photometric uncertainties if $\beta > 1$.

In a second model-fitting run we corrected for smooth trends of the light curves. Ground-based differential photometry light curves of transit events typically show such a trend over time caused by a colour difference between the exoplanet host star and the comparison stars. To determine whether a linear or a quadratic detrending polynomial in time is a sufficient description for the trend, we used the Bayesian information criterion BIC (Schwarz 1978). The BIC penalises free parameters and therefore balances an increase in the likelihood with the number of parameters used in the model. The model with the lowest BIC is preferred. In most of the analysed broad band light curves the trend is well described by a linear trend (see Table A.2). All
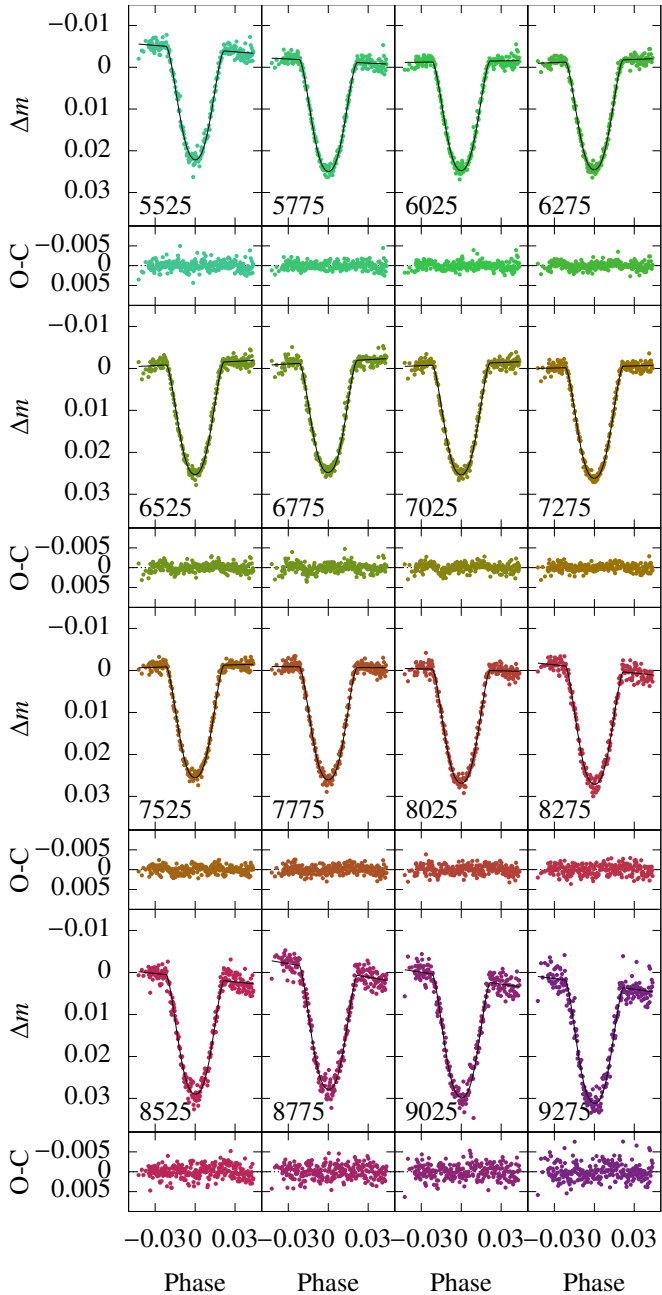
Fig. 3. Sixteen channel GTC light curves. *Upper panels*: light curves with best fit model in black. Labels indicate the middle of the spectral bin, each with a spectral width of 250 Å. *Lower panels*: residuals of best fit model.

light curves obtained at the GTC are well described by a linear trend.

We performed a final fit with the obtained enlarged uncertainties and the determined detrending polynomial. Because no cosmic ray correction was applied in the reduction of the GTC-spectra, we applied a 5σ-clipping to the residuals of the light curves after a first fit with JKTEBOP. The final model fitting contains the planetary radius and the polynomial coefficients as free parameters. The parameter uncertainties were obtained with JKTEBOP using both a Monte Carlo simulation with 5000 steps and a residual permutation method. For each spectral bin, we adopted the method that yields the largest uncertainty in the radius. The results of the light curve analysis

are listed in Table A.2. Figure 3 shows modelled light curves of the GTC/OSIRIS spectra. Figures 4–6 show the broad band light curves. An overview of the measured radius ratios for the broad band light curves is presented in Fig. 7.

Next, we fitted all broad band light curves of one band simultaneously with JKTEBOP using again enlarged error-bars as described above. JKTEBOP allows for a simultaneous fit of multiple transit observations if one common LD function can be applied. The software cannot handle different LDCs to subsamples of the input data, which prohibits the simultaneous fit of multi-colour data. However, JKTEBOP is able to assign independent detrending polynomials to the individual light curves, so that the detrending is included in the transit fit.

5. Results

5.1. Transit depth as a function of wavelength

The combined transmission spectrum for TrES-3 b of broad band observations and the newly analysed GTC/OSIRIS data is shown in Fig. 8. Additionally, the figure contains the GTC results derived by P16. Our work cannot reproduce the strong slope found by P16 of 25.9 ± 4.7 scale heights from ~5500 to 7500 Å. We compare the weighted mean of the three bluest wavelength bins 5525 Å, 5775 Å, and 6025 Å to the central bins of 7275 Å, 7575 Å, and 7775 Å . In P16, they exhibit a difference of 19.5 ± 2.9 scale heights. The weighted mean of the same spectral bins for the reanalysed GTC data of this work show a difference of 5.7 ± 1.7 scale heights. A comparison of the broad band data for similar wavelength ranges shows a difference of 4.0 ± 1.9 scale heights between the weighted mean of the *RISE*, *r'* and *R* band and the *I* band.

The broad band data alone do not exhibit a significant wavelength dependence of R_p/R_*. The weighted mean of the nine band passes is $k = 0.1678 \pm 0.0004$, and the reduced χ^2 of all nine measurements compared to that mean is 1.41, being sufficiently close to unity to be in reasonable agreement with a flat spectrum.

We compared the derived broad band spectrophotometry and spectroscopic transmission spectrum of this work with theoretical models produced with an existing radiative transfer model (García Muñoz et al. 2012; Nielsen et al. 2016). The methodology is similar to that followed in Sedaghati et al. (2016). The models assume that the planet atmosphere is dominated by H_2/He, and includes as minor gases H_2O (volume mixing ratio $vmr = 10^{-3}$, independent of altitude), Na ($vmr = 2.96 \times 10^{-6}$), and K ($vmr = 2.4 \times 10^{-4}$). The background number density of the gas is determined by solving the hydrostatic balance equation with an altitude-dependent gravity from 10^3 to 10^{-7} bar. The temperature is assumed constant throughout the atmosphere and equal to 1700 K.

We include extinction from the gas in the form of Rayleigh scattering and molecular/atomic absorption, as well as extinction from a postulated haze. The H_2O linelist of optical properties is from the HITEMP database (Rothman et al. 2010). For the alkalis, we implemented the parametrisation of absorption given in Iro et al. (2005). For the haze, our nominal (x1) scenario assumes the following variation of the extinction coefficient (in cm^{-1}) with altitude at a wavelength of $1\,\mu m$, $\gamma(z; \lambda = 1\,\mu m) = 4.1 \times 10^{-7} \exp(-z/H_a)$. At other wavelengths, we corrected according to a Rayleigh law, $\gamma(z; \lambda) = \gamma(z; \lambda = 1\,\mu m)(1/\lambda[\mu m])^4$. For the x0 (clear) and x1000 (hazy) scenarios (see Fig. 9), we multiplied $\gamma(z; \lambda)$ by 0 or by 1000, respectively. Altitude z is

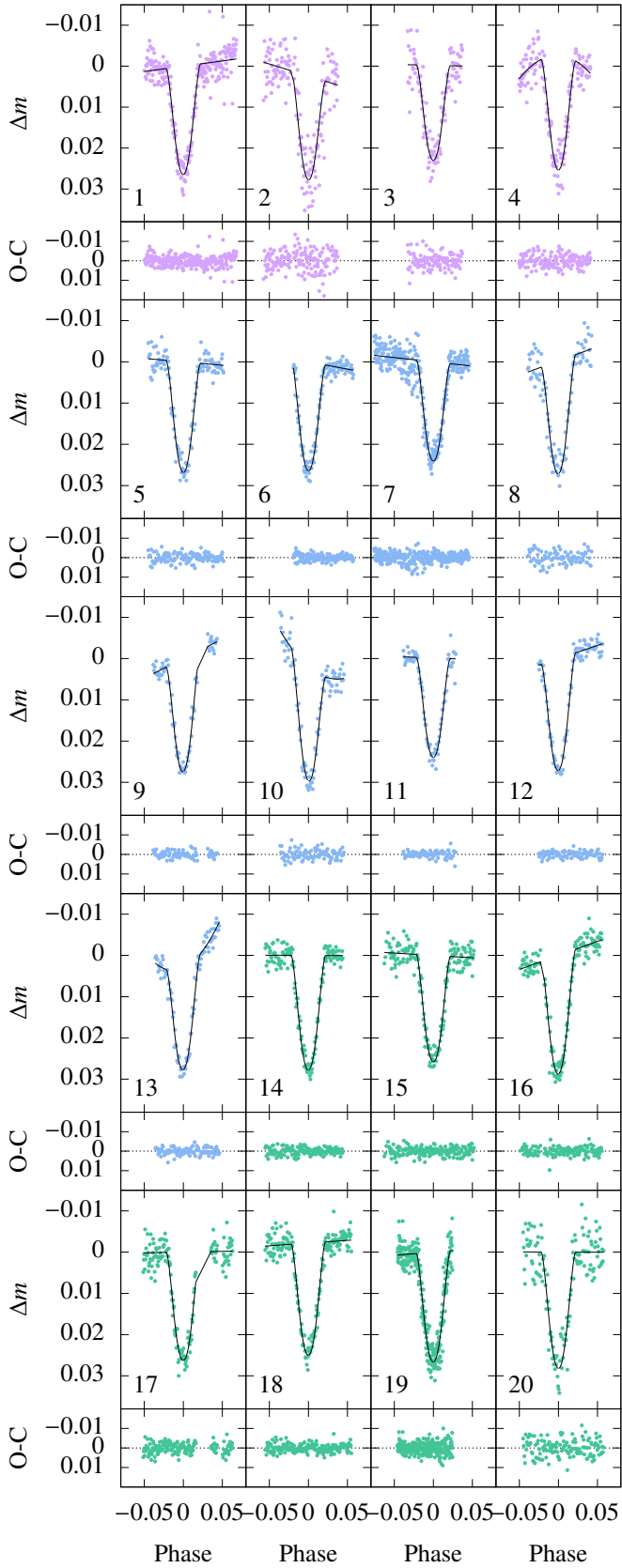**Fig. 4.** Broad band light curves I. Light curves are sorted by the observation number given in Table A.2. *Upper panels*: differential magnitude as a function of orbital phase. The black line shows the best fit model. *Lower panels*: residuals of the best fit model.
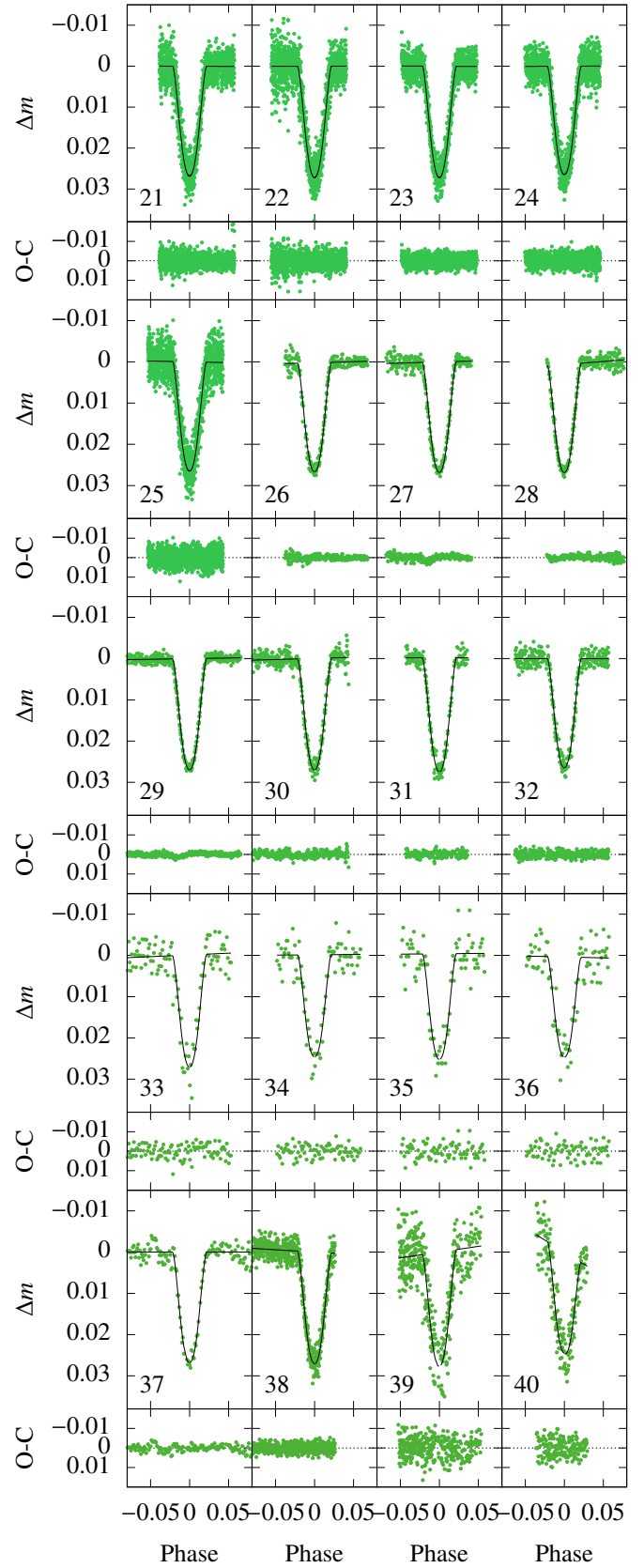
Fig. 5. Broad band light curves II. Light curves are sorted by the observation number given in Table A.2. This plot is a continuation of Fig. 4.
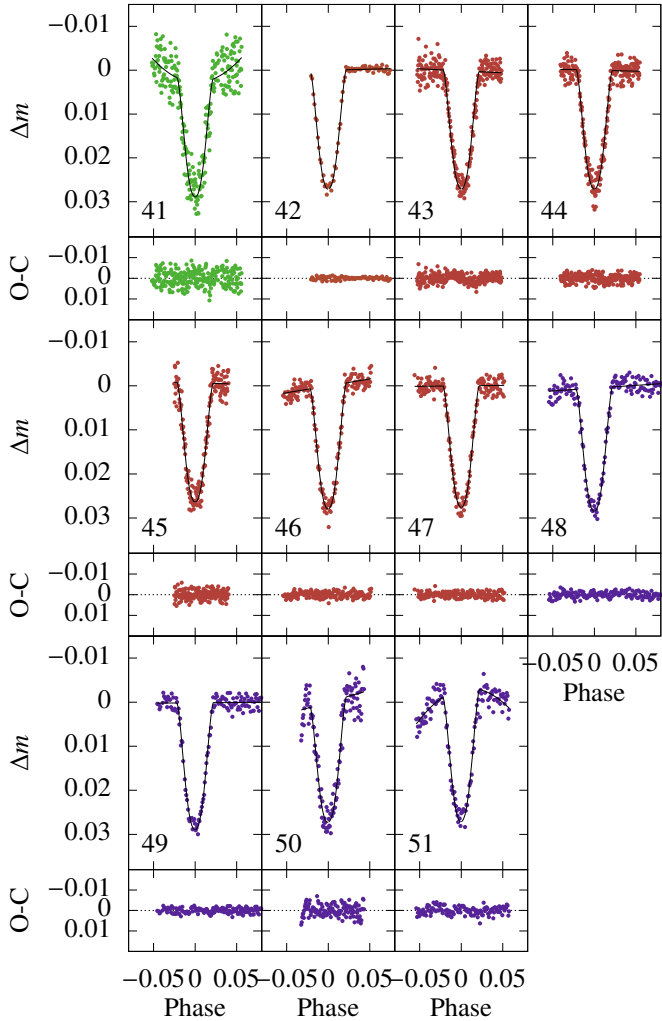
Fig. 6. Broad band light curves III. Light curves are sorted by the observation number given in Table A.2. This plot is a continuation of Fig. 5.

measured with respect to the pressure level of 10^3 bar. We assumed $H_a = 250$ km for the scale height of the haze, which is comparable to the scale height of the gas.

The synthetic spectra were binned to the same wavelength channels and filter curves as our measurements. The vertical offset, as the only remaining parameter, was fitted to measurements using the least squares method. For each model we calculated the χ^2 value and the probability P of the χ^2 test, that is, the probability that the measurements could result from statistical fluctuations alone in case the model is true. The values are summarised in Table 5.

Both models show smaller variations in the radius ratio than our data and are ruled out by the data according to their P values. For comparison, we also included a wavelength-independent radius ratio which represents an atmosphere dominated by clouds (flat model) and a linear function with slope of increased absorption towards shorter wavelength. None of the models is in agreement with our combined GTC and broad band data. The main cause is the R_p/R_* variation within the GTC data, and therefore relies on a single transit observation, while the multi-epoche multi-telescope broad band observations agree within their uncertainties to the models (but cannot differentiate between them). Repeated long-slit or multi-object spectroscopic transit observations would be beneficial to confirm the GTC data.

5.2. Stellar activity

Unocculted star spots mimic a negative slope in the optical transmission spectrum (Sing et al. 2011; Pont et al. 2013; Oshagh et al. 2014). TrES-3 is classified as a moderately active star according to the CaII H & K line strengths ($\log(R_{HK}) = -4.54$, Sozzetti et al. 2009; Knutson et al. 2010), however, to our knowledge no photometric out-of-transit variation was reported yet in the literature. We monitored the host star to deduce an upper limit on the star spot coverage and their effect on the transmission spectrum from its photometric variability. Similar photometric monitoring campaigns for different targets are presented, for example, in Mallonn et al. (2015b) and Mallonn & Strassmeier (2016). The Lomb-Scargle periodograms in Fig. 2 show no peaks at a false alarm probability (FAP) of below 0.01, thus no significantly periodic variation was detected (looking for periods of 1 to 100 days). Fitting sine curves to the light curves with frequencies fixed at the highest peaks in the periodograms results in semi-amplitudes below 4.5 mmag. We conclude that our monitoring data rule out periodic variations higher than this value.

The modification of the depth of a transit light curve is directly related to the photometric variation caused by unocculted spots. A decrease of 1 per cent in stellar flux increases the derived transit depth by about 1 per cent in relative units (Sing et al. 2011). During our multi-epoch transit observations the stellar flux varied by less than 1 percent. Thus, we derive an upper limit of spot-caused uncertainty in the radius ratio k of 0.0008. This value approximately equals our best transit fit uncertainties for k. However, the wavelength-dependent effect on the transmission spectrum is about an order of magnitude smaller for solar-type host stars (depending on the temperature contrast of the spot and the quiet photosphere) than this absolute effect (Sing et al. 2011; Mallonn et al. 2015b). One scale height for TrES-3 b equals approximately $\Delta k \sim 0.0004$, and the upper limit of a star-spot effect is less than that value. Therefore, we can neglect any influence of potentially present unocculted star spots on the broad band transmission spectrum derived here. It is unlikely that spots significantly modify the results of the GTC data.

6. Summary and conclusion

In this work we investigate the transmission spectrum of the Hot Jupiter TrES- 3b. We follow-up on a result published by P16 who reported an overly large Rayleigh-like feature. We reanalyse the GTC spectroscopic transit observation used by P16 and complement these data by a large sample of published and newly acquired broad band observations in nine different pass bands. We use more than 50 individual broad band light curves from the near-UV to the near-infrared. All light curves are analysed homogeneously and simultaneously per filter to avoid systematic error and reduce the final uncertainties.

Due to the almost grazing orbit of TrES-3 b we did not fit the LDCs but rely on theoretical values. While for the majority of exoplanet host stars the theoretical LDCs agree reasonably well with their measured counterparts (Müller et al. 2013), there are known cases of discrepant values, for example HD 209458 (Claret 2009) and HAT-P-32 (Mallonn & Strassmeier 2016).

In the transmission spectrum, both the newly analysed GTC data and the multi-colour broad band data rule out the very large feature found in the transmission spectrum by P16. This allows us to disprove the suggested overly large Rayleigh-like feature in our analysis. In the new analysis the increase of 10.8 ± 3.6 scale
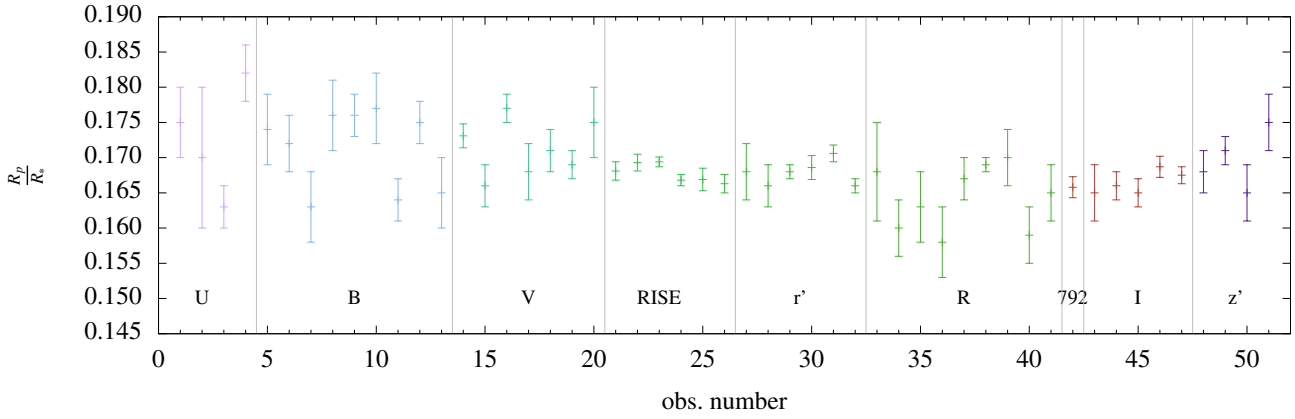
Fig. 7. Radius ratios of broad band observations. They are sorted by the observation number given in Table A.1. All vertical error-bars indicate the 1σ uncertainty.
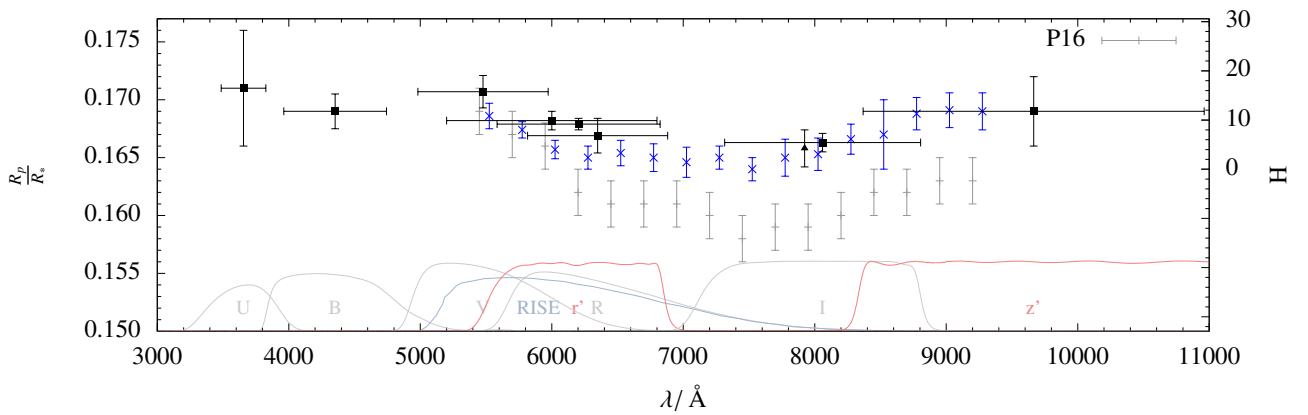

Fig. 8. Transmission spectrum of TrES-3 b. Shown is the GTC/OSIRIS spectrum (crosses). The broadband photometry is indicated with squares. The response function for each photometric band is shown at the bottom. Horizontal error-bars indicate the FWHM of the band. The narrow band observations by Colón et al. (2010) are indicated with a triangle. The results of the previous study by P16, their Fig. 9, are shown for comparison with an arbitrary offset of -75 Å for clarity. All vertical error-bars indicate the 1σ uncertainty.
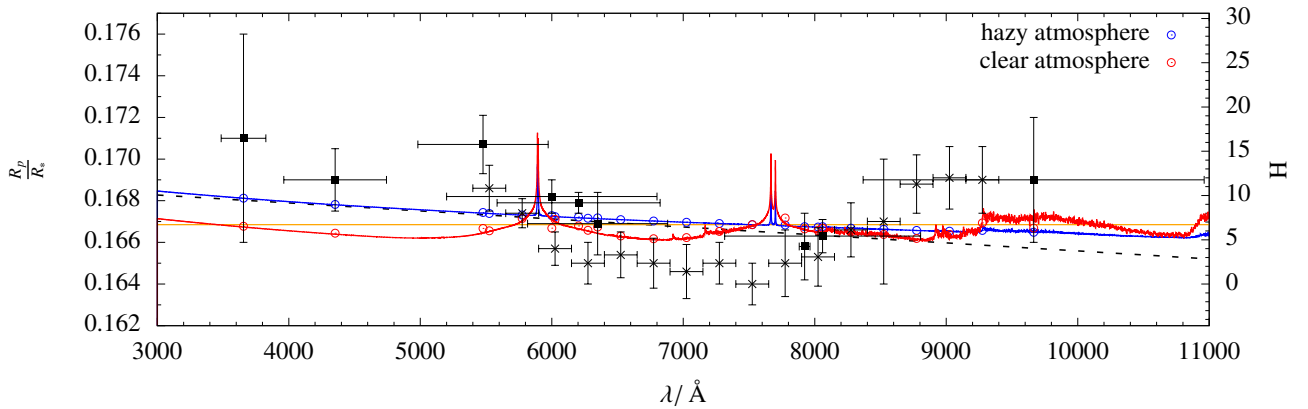
Fig. 9. Model atmospheres for a clear and an atmosphere with haze fitted to the transmission spectrum of TrES-3b. The measurements are plotted in black. The binned model data are indicated as coloured circles. Additionally, a constant (orange solid line) and a linear best fit (dashed black line) are shown.

heights between 5525 Å and 7525 Å is of much lower amplitude than for the measurements by P16 with 25.9 ± 4.7 scale heights. Since this intriguing feature is based on a single transit observation and disagrees with the r' band as our most precise broad band measurement by 3σ, we suggest a repetition of the spectroscopic transit observation to verify this signal. From our analysis we conclude the overly large Rayleigh-like feature is not intrinsic to the TrES-3 system.

For comparison we also analysed the GTC stellar spectra reduced by P16 which are available publicly[2]. We extracted the transit light curves from these 1D spectra of TrES-3 b and comparison star and performed the light curve analysis as described in Sect. 4. The resulting transmission spectrum shows a slope

---

[2] https://github.com/hpparvi/Parviainen-2015-TrES-3b-OSIRIS

Table 3. Measured radius ratios of the broad band observations.

Band	$\lambda\,/\,\text{Å}$	R_p/R_*
U	3656 ± 170	0.171 ± 0.005
B	4353 ± 390.5	0.1690 ± 0.0015
V	5477 ± 495.5	0.1707 ± 0.0014
RISE	6000 ± 800	0.1682 ± 0.0008
r'	6204 ± 620	0.1679 ± 0.0005
R	6349 ± 532.8	0.1669 ± 0.0015
792	7923 ± 41	0.1658 ± 0.0016
I	8060 ± 745	0.1663 ± 0.0008
z'	9665 ± 1297	0.169 ± 0.003

Notes. The columns show the photometric band, their corresponding central wavelength and FWHM, as well as the radius ratio with 1σ uncertainty.

Table 4. Measured radius ratios for the GTC/OSIRIS spectra.

$\lambda\,/\,\text{Å}$	R_p/R_*	β
5525 ± 125	0.1686 ± 0.0011	1.19
5775 ± 125	0.1674 ± 0.0007	1.13
6025 ± 125	0.1657 ± 0.0008	1.26
6275 ± 125	0.165 ± 0.001	1.39
6525 ± 125	0.1654 ± 0.0011	1.42
6775 ± 125	0.1650 ± 0.0012	1.52
7025 ± 125	0.1646 ± 0.0013	1.47
7275 ± 125	0.165 ± 0.001	1.15
7525 ± 125	0.164 ± 0.001	1.30
7775 ± 125	0.1650 ± 0.0016	1.35
8025 ± 125	0.1653 ± 0.0014	1.32
8275 ± 125	0.1666 ± 0.0013	1.24
8525 ± 125	0.167 ± 0.003	1.29
8775 ± 125	0.1688 ± 0.0014	1.21
9025 ± 125	0.1691 ± 0.0015	1.04
9275 ± 125	0.1690 ± 0.0016	1.15

Notes. The columns show the centre of the spectral bin, its width, and the radius ratio with 1σ uncertainty and the β-factor.

very similar to P16 except for being vertically offset compared to P16. This offset might be caused by systematic differences in the limb darkening coefficient from the different calculations by P16 and Claret et al. (2013). Since the large variation in the transmission spectrum of P16 is reproduced when we analyse their reduced data, we suggest that the origin of the discrepancy in the GTC transmission spectrum between P16 and this work is not to be found in the analysis, but in the data reduction. The two versions of the data reduction of this work and P16 differ in details of the flux extraction and the wavelength calibration, but it was not possible to clarify what detail was responsible.

Our long-term photometric monitoring rules out a significant modification of the derived transmission spectrum in this work by unoccluded star spots. The relative amplitudes induced by stellar activity are smaller than the uncertainties of our radius ratio measurements. Therefore, unoccluded spots cannot introduce a spectral slope in the transmission spectrum at the current level of measurement precision.

Still the measurements cannot distinguish between individual atmospheric model spectra because TrES-3 b is a moderately favourable target for transmission spectroscopy due to its small scale height. We showed the Rayleigh-like feature of approximately 26 scale heights is not reproducible.

Table 5. χ^2_{red} and one-tailed probability *P* for the fitted atmospheric models using the complete data set and the broad band measurements only.

Model	GTC + broad band		Broad band	
	χ^2_{red}	*P*	χ^2_{red}	*P*
clear	2.34	0.000213	1.43	0.177803
haze	2.13	0.001029	1.47	0.160381
constant	2.29	0.000644	1.41	0.189385
linear	2.23	0.000325	0.69	0.683219

References

Bertin, E., & Arnouts, S. 1996, A&AS, 117, 393
Broeg, C., Fernández, M., & Neuhäuser, R. 2005, Astron. Nachr., 326, 134
Burrows, A. S. 2014, Proc. National Academy of Science, 111, 12601
Christiansen, J. L., Ballard, S., Charbonneau, D., et al. 2011, ApJ, 726, 94
Claret, A. 2000, A&A, 363, 1081
Claret, A. 2009, A&A, 506, 1335
Claret, A., Hauschildt, P. H., & Witte, S. 2013, A&A, 552, A16
Colón, K. D., Ford, E. B., Lee, B., Mahadevan, S., & Blake, C. H. 2010, MNRAS, 408, 1494
Dragomir, D., Benneke, B., Pearson, K. A., et al. 2015, ApJ, 814, 102
Eastman, J., Siverd, R., & Gaudi, B. S. 2010, PASP, 122, 935
Ehrenreich, D., Bourrier, V., Wheatley, P. J., et al. 2015, Nature, 522, 459
Espinoza, N., & Jordán, A. 2015, MNRAS, 450, 1879
Evans, T. M., Sing, D. K., Wakeford, H. R., et al. 2016, ApJ, 822, L4
Fortney, J. J., Shabram, M., Showman, A. P., et al. 2010, ApJ, 709, 1396
Fraine, J., Deming, D., Benneke, B., et al. 2014, Nature, 513, 526
García Muñoz, A., Zapatero Osorio, M. R., Barrena, R., et al. 2012, ApJ, 755, 103
Gibson, N. P., Pollacco, D., Simpson, E. K., et al. 2009, ApJ, 700, 1078
Gibson, N. P., Nikolov, N., Sing, D. K., et al. 2017, MNRAS, 467, 4591
Iro, N., Bézard, B., & Guillot, T. 2005, A&A, 436, 719
Jiang, I.-G., Yeh, L.-C., Thakur, P., et al. 2013, AJ, 145, 68
Kirk, J., Wheatley, P. J., Louden, T., et al. 2016, MNRAS, 463, 2922
Knutson, H. A., Howard, A. W., & Isaacson, H. 2010, ApJ, 720, 1569
Kreidberg, L., Bean, J. L., Désert, J.-M., et al. 2014, Nature, 505, 69
Kreidberg, L., Line, M. R., Bean, J. L., et al. 2015, ApJ, 814, 66
Kundurthy, P., Becker, A. C., Agol, E., Barnes, R., & Williams, B. 2013, ApJ, 764, 8
Lee, J. W., Youn, J.-H., Kim, S.-L., Lee, C.-U., & Koo, J.-R. 2011, PASJ, 63, 301
Lendl, M., Delrez, L., Gillon, M., et al. 2016, A&A, 587, A67
Madhusudhan, N., Knutson, H., Fortney, J. J., & Barman, T. 2014, Protostars and Planets VI, 739
Mallonn, M., & Strassmeier, K. G. 2016, A&A, 590, A100
Mallonn, M., Nascimbeni, V., Weingrill, J., et al. 2015a, A&A, 583, A138
Mallonn, M., von Essen, C., Weingrill, J., et al. 2015b, A&A, 580, A60
Mancini, L., Ciceri, S., Chen, G., et al. 2013, MNRAS, 436, 2
Mancini, L., Southworth, J., Ciceri, S., et al. 2014, MNRAS, 443, 2391
Miller-Ricci, E., & Fortney, J. J. 2010, ApJ, 716, L74
Müller, H. M., Huber, K. F., Czesla, S., Wolter, U., & Schmitt, J. H. M. M. 2013, A&A, 560, A112
Murgas, F., Pallé, E., Zapatero Osorio, M. R., et al. 2014, A&A, 563, A41
Nascimbeni, V., Mallonn, M., Scandariato, G., et al. 2015, A&A, 579, A113
Ngo, H., Knutson, H. A., Hinkley, S., et al. 2015, ApJ, 800, 138
Nielsen, L. D., Ferruit, P., Giardino, G., et al. 2016, in Space Telescopes and Instrumentation 2016: Optical, Infrared, and Millimeter Wave, Proc. SPIE, 9904, 99043
Nikolov, N., Sing, D. K., Gibson, N. P., et al. 2016, ApJ, 832, 191
O'Donovan, F. T., Charbonneau, D., Bakos, G. Á., et al. 2007, ApJ, 663, L37
Oshagh, M., Santos, N. C., Boisse, I., et al. 2013, A&A, 556, A19
Oshagh, M., Santos, N. C., Ehrenreich, D., et al. 2014, A&A, 568, A99
Palle, E., Chen, G., Alonso, R., et al. 2016, A&A, 589, A62
Parviainen, H., Pallé, E., Nortmann, L., et al. 2016, A&A, 585, A114

Pont, F., Zucker, S., & Queloz, D. 2006, MNRAS, 373, 231
Pont, F., Sing, D. K., Gibson, N. P., et al. 2013, MNRAS, 432, 2917
Rothman, L. S., Gordon, I. E., Barber, R. J., et al. 2010, J. Quant. Spectr. Rad. Transf., 111, 2139
Sada, P. V., Deming, D., Jennings, D. E., et al. 2012, PASP, 124, 212
Schwarz, G. 1978, Ann. Statist., 6, 461
Seager, S., Deming, D., & Valenti, J. A. 2009, Astrophysics and Space Science Proc., 10, 123
Sedaghati, E., Boffin, H. M. J., Jeřabková, T., et al. 2016, A&A, 596, A47
Seeliger, M., Dimitrov, D., Kjurkchieva, D., et al. 2014, MNRAS, 441, 304
Sing, D. K. 2010, A&A, 510, A21
Sing, D. K., Pont, F., Aigrain, S., et al. 2011, MNRAS, 416, 1443
Sing, D. K., Huitson, C. M., Lopez-Morales, M., et al. 2012, MNRAS, 426, 1663
Sing, D. K., Fortney, J. J., Nikolov, N., et al. 2016, Nature, 529, 59
Snellen, I. A. G., Albrecht, S., de Mooij, E. J. W., & Le Poole, R. S. 2008, A&A, 487, 357
Southworth, J. 2008, MNRAS, 386, 1644
Southworth, J. 2011, MNRAS, 417, 2166
Southworth, J., & Evans, D. F. 2016, MNRAS, 463, 37
Southworth, J., Maxted, P. F. L., & Smalley, B. 2004, MNRAS, 351, 1277
Southworth, J., Mancini, L., Ciceri, S., et al. 2015, MNRAS, 447, 711
Southworth, J., Mancini, L., Madhusudhan, N., et al. 2017, AJ, 153, 191
Sozzetti, A., Torres, G., Charbonneau, D., et al. 2009, ApJ, 691, 1145
Strassmeier, K. G. 2009, A&ARv, 17, 251
Strassmeier, K. G., Granzer, T., Weber, M., et al. 2004, Astron. Nachr., 325, 527
Teske, J. K., Turner, J. D., Mueller, M., & Griffith, C. A. 2013, MNRAS, 431, 1669
Turner, J. D., Smart, B. M., Hardegree-Ullman, K. K., et al. 2013, MNRAS, 428, 678
Turner, J. D., Pearson, K. A., Biddle, L. I., et al. 2016, MNRAS, 459, 789
Vaňko, M., Maciejewski, G., Jakubík, M., et al. 2013, MNRAS, 432, 944
Vidal-Madjar, A., Lecavelier des Etangs, A., Désert, J.-M., et al. 2003, Nature, 422, 143
Wakeford, H. R., & Sing, D. K. 2015, A&A, 573, A122
Winn, J. N., Holman, M. J., Torres, G., et al. 2008, ApJ, 683, 1076
Wood, P. L., Maxted, P. F. L., Smalley, B., & Iro, N. 2011, MNRAS, 412, 2376

Appendix A: Additional tables

Table A.1. Overview of the analysed transit observations of TrES-3 b.

Band	Ref.	Date of obs.	Cadence /s	N_{data}	rms /mmag	#
U	1	2016-04-25	40	253	2.73	1
	2	2011-10-14	67	151	5.03	2
	2	2011-11-04	67	115	3.59	3
	2	2012-03-25	69	151	3.20	4
B	3	2016-05-02	45	121	2.19	5
	4	2007-04-08	70	126	1.53	6
	2	2012-04-11	47	314	2.41	7
	5	2016-04-12	102	91	3.01	8
	5	2016-04-25	102	77	1.65	9
	5	2016-05-19	102	91	2.39	10
	5	2016-06-01	102	75	1.64	11
	5	2016-06-05	102	90	1.49	12
	5	2016-06-18	102	92	2.09	13
V	6	2007-04-24	82	139	1.72	14
	7	2016-03-09	69	172	2.12	15
	7	2016-04-29	69	146	1.94	16
	7	2016-05-02	69	147	2.57	17
	7	2016-05-19	69	181	1.96	18
	2	2009-07-04	30	270	2.81	19
	8	2016-04-19	90	130	4.14	20
RISE	9	2008-03-08	8	1350	2.92	21
	9	2008-05-28	8	1350	3.39	22
	9	2008-06-14	8	1350	2.18	23
	9	2008-07-01	8	1350	2.48	24
	9	2008-07-22	8	1350	3.27	25
r'	10	2009-05-14	45	238	1.16	26
	10	2010-05-16	45	248	1.23	27
	10	2010-10-12	45	246	1.09	28
	10	2011-03-24	45	371	0.74	29
	10	2011-06-21	45	306	1.43	30
	10	2011-08-24	45	168	1.34	31
	6	2008-03-27	44	291	1.48	32
R	11	2010-05-25	100	99	3.45	33
	11	2010-06-11	100	80	2.95	34
	11	2010-06-15	100	80	3.70	35
	11	2010-06-28	100	77	3.69	36
	12	2010-06-15	100	158	1.70	37
	2	2009-06-22	21	581	1.80	38
	13	2009-08-01	45	345	4.95	39
	13	2010-04-27	35	180	4.17	40
	13	2010-06-30	40	238	3.68	41
792	14	2009-08-10	140	71	0.68	42
I	6	2008-03-09	44	253	2.01	43
	6	2008-03-27	44	246	1.75	44
	6	2008-04-12	63	166	2.14	45
	7	2016-07-19	69	169	1.34	46
	7	2016-08-25	69	171	1.33	47
z'	4	2007-03-26	150	150	1.41	48
	6	2007-03-25	104	134	1.24	49
	5	2016-06-28	72	119	2.84	50
	5	2016-07-15	102	125	1.85	51

Notes. Columns are the photometric band, source reference (if applicable), date of observation, cadence, number of data points N_{data} and dispersion of the residuals as root mean square (rms) of the observations after subtracting a transit model. The last column indicates the observation number.

References. (1) TNG; (2) Turner et al. (2013); (3) CAHA; (4) O'Donovan et al. (2007); (5) STELLA; (6) Sozzetti et al. (2009); (7) T1T; (8) VBO; (9) Gibson et al. (2009); (10) Kundurthy et al. (2013); (11) Jiang et al. (2013); (12) Lee et al. (2011); (13) Vaňko et al. (2013); (14) Colón et al. (2010).

Table A.2. Results of the individual broad band observations.

Band	Reference	Date of obs.	R_P/R_*	β	Detrend	#
U	1	2016-04-25	0.175 ± 0.005	1.17	linear	1
	2	2011-10-14	0.17 ± 0.01	1.21	linear	2
	2	2011-11-04	0.163 ± 0.003	1.00	linear	3
	2	2012-03-25	0.182 ± 0.004	1.24	quadratic	4
B	3	2016-05-02	0.174 ± 0.005	1.08	linear	5
	4	2007-04-08	0.172 ± 0.004	1.09	linear	6
	2	2012-04-11	0.163 ± 0.005	1.36	linear	7
	5	2016-04-12	0.176 ± 0.005	1.13	linear	8
	5	2016-04-25	0.176 ± 0.003	1.00	linear	9
	5	2016-05-19	0.185 ± 0.004	1.14	quadratic	10
	5	2016-06-01	0.164 ± 0.003	1.00	linear	11
	5	2016-06-05	0.175 ± 0.003	1.08	linear	12
	5	2016-06-18	0.179 ± 0.005	1.23	quadratic	13
V	6	2007-04-24	0.1731 ± 0.0017	1.13	linear	14
	7	2016-03-09	0.166 ± 0.003	1.14	linear	15
	7	2016-04-28	0.177 ± 0.002	1.06	linear	16
	7	2016-05-02	0.168 ± 0.004	1.19	linear	17
	7	2016-05-19	0.171 ± 0.003	1.16	linear	18
	2	2009-07-04	0.169 ± 0.002	1.04	linear	19
	8	2016-04-19	0.175 ± 0.005	1.09	linear	20
RISE	9	2008-03-08	0.1681 ± 0.0013	1.02	linear	21
	9	2008-05-28	0.1693 ± 0.0012	1.00	linear	22
	9	2008-06-14	0.1694 ± 0.0007	1.09	linear	23
	9	2008-07-01	0.1668 ± 0.0008	1.00	linear	24
	9	2008-07-22	0.1669 ± 0.0016	1.43	linear	25
r'	10	2009-05-14	0.1663 ± 0.0013	1.08	linear	26
	10	2010-05-16	0.168 ± 0.004	1.62	linear	27
	10	2010-10-12	0.166 ± 0.003	1.36	linear	28
	10	2011-03-24	0.168 ± 0.001	1.55	linear	29
	10	2011-06-21	0.1686 ± 0.0017	1.40	linear	30
	10	2011-08-24	0.1706 ± 0.0012	1.11	linear	31
	6	2008-03-27	0.166 ± 0.001	1.08	linear	32
R	11	2010-05-25	0.168 ± 0.007	1.10	linear	33
	11	2010-06-11	0.160 ± 0.004	1.00	linear	34
	11	2010-06-15	0.163 ± 0.005	1.06	linear	35
	11	2010-06-28	0.158 ± 0.005	1.04	linear	36
	12	2010-06-15	0.167 ± 0.003	1.32	linear	37
	2	2009-06-22	0.169 ± 0.001	1.00	linear	38
	13	2009-08-01	0.170 ± 0.004	1.08	linear	39
	13	2010-04-27	0.159 ± 0.004	1.05	linear	40
	13	2010-06-30	0.177 ± 0.006	1.27	quadratic	41
792	14	2009-08-10	0.1658 ± 0.0015	1.00	linear	42
I	6	2008-03-09	0.165 ± 0.004	1.43	linear	43
	6	2008-03-27	0.166 ± 0.002	1.24	linear	44
	6	2008-04-12	0.165 ± 0.002	1.10	linear	45
	7	2016-07-18	0.1687 ± 0.0015	1.12	linear	46
	7	2016-08-25	0.1675 ± 0.0012	1.01	linear	47
z'	4	2007-03-26	0.168 ± 0.003	1.26	linear	48
	6	2007-03-25	0.171 ± 0.002	1.11	linear	49
	5	2016-06-28	0.165 ± 0.004	1.18	linear	50
	5	2016-07-15	0.163 ± 0.007	1.46	quadratic	51

Notes. Columns are the photometric band, source reference (if applicable), the date of observation, as well as the radius ratio, β-factor and used order of the detrending polynomial over time. The last column indicates the observation number.

References. (1) TNG; (2) Turner et al. (2013); (3) CAHA; (4) O'Donovan et al. (2007); (5) STELLA; (6) Sozzetti et al. (2009); (7) T1T; (8) VBO; (9) Gibson et al. (2009); (10) Kundurthy et al. (2013); (11) Jiang et al. (2013); (12) Lee et al. (2011); (13) Vaňko et al. (2013); (14) Colón et al. (2010)